

Energy-Transfer-Enhanced Emission and Quantum Sensing of V_{B^-} Defects in hBN–PbI₂ Heterostructures

E. Mayner¹, Ya. Zhumagulov², C. de Giorgio³, F. Chu¹, P. Swain⁴, G. Fantner⁴, A. Kis³, O. Yazyev², A. Radenovic¹

¹ LBEN, Institute of Biotechnology, École Polytechnique Fédérale de Lausanne (EPFL), CH-1015 Lausanne, Switzerland.

² C3MP, École Polytechnique Fédérale de Lausanne (EPFL), Institute of Physics, 1015, Lausanne, Switzerland

³ LANES, Electrical Engineering Institute, École Polytechnique Fédérale de Lausanne (EPFL), CH-1015 Lausanne, Switzerland

⁴ LBNI, Institute of Biotechnology, École Polytechnique Fédérale de Lausanne (EPFL), CH-1015 Lausanne, Switzerland.

Email: eveline.mayner@epfl.ch, aleksandra.radenovic@epfl.ch

ABSTRACT

Spin defects in two-dimensional materials hold significant potential for quantum information technologies and sensing applications. The negatively charged boron vacancy (V_{B^-}) in hexagonal boron nitride (hBN) has attracted considerable attention as a quantum sensor due to its demonstrated sensitivity to temperature, magnetic fields, and pressure.¹ However, its applications have thus far been limited by inherently dim photoluminescence (PL). By fabricating a van der Waals heterostructure with a sensitizing donor layer, lead iodide (PbI₂), we effectively enhance the PL intensity from the V_{B^-} by 5–45×, while maintaining compatibility with other heterostructures and vdW optoelectronic platforms. The type-I band alignment at the heterojunction enables efficient exciton migration while suppressing back-electron transfer, and the strong spectral overlap between the PbI₂ emission and defect absorption supports efficient fluorescence resonance energy transfer. Ab initio density functional theory (DFT) predicts a photon-ratcheting mechanism that boosts absorption and emission while maintaining magnetic resonance (ODMR) contrast through minimal hybridization. Experimentally, the heterostructure exhibits enhanced continuous-wave ODMR sensitivity and functions as a precise probe of external magnetic fields. This work establishes a proof-of-concept for amplifying weak defect signals in nanomaterials, highlighting a new strategy for engineering their optical and magnetic responses.

INTRODUCTION

Optically addressable spin defects in solids have emerged as promising platforms for quantum photonic information processing^{2–5} and sensing.^{6,7} Quantum sensing based on these platforms has proven effective across applications and device scales, from detecting individual nuclear spins⁸ to measuring currents in full battery systems.⁹ Color centers in silicon carbide^{10–12} and in diamond^{2,13–15} are well-studied defect platforms for quantum technologies⁴ and NV (diamond-based) centers have already been integrated into CMOS-compatible devices.¹⁶ However, the bulk three-dimensional nature of diamond and silicon carbide limits their integration into planar device architectures, and in diamond in particular, device miniaturization introduces trade-offs between spatial scaling and noise performance, and susceptibility to uncontrolled surface functionalization.^{17,18}

Alternatively, optical readout of spin defects in two-dimensional (2D) layered materials has a variety of fundamental and technological benefits for quantum applications.^{19,20} For quantum sensing, the nanoscale proximity of the probe to the target allows for high-sensitivity and high-resolution quantum sensing. In contrast to diamonds, hBN offers an atomically clean surface with minimal dangling bonds and charge traps.²¹ The flat nature also aids in facile compatibility with optoelectronic devices. hBN has long been used as an encapsulation layer or gate dielectric material in vdW electronics.^{22–25} Thus, introducing a V_B[–] sensing layer with nanoscale proximity would require no additional fabrication complexity, while offering information on the local physics of the devices. In this vein, V_B[–] in hBN has already been used for widefield sensing of another vdW material²⁶ and, given the wide library of 2D materials, there is an immense opportunity for engineering devices and the sensitivity of 2D sensors.^{27–29}

Control of the spin-photon interface has been realized in hBN with several defect candidates, including the negatively charged boron vacancy (V_B[–])^{30–35} and a carbon-related^{36,37,8,38} defects. One such method of spin-photon polarization and readout is optically detected magnetic resonance (ODMR): The defect is polarized to the high-spin ground or excited state, and the state is read out via the spin-dependent rates of excitation, decay, and intersystem crossing available to the system. ODMR allows one to sense with optical readout the magnetic field, electric field, strain, temperature, and pressure.^{1,31,39}

High-sensitivity ODMR and widefield ODMR both require high PL signals. However, despite its flatness making it a natural choice for sensing in optoelectronic devices and widefield sensing, the V_B[–] as a sensor suffers from several factors currently limiting its applicability. This includes fast decoherence^{32,40,41} and low brightness.^{42,43} To address the low coherence times, dynamic decoupling spin sequences have been used^{40,44} as well as studies varying the density of defects^{40,45} and depth.⁴⁶ The density was revealed to be inversely proportional to coherence time, T_{2,XY-8}.⁴⁰ However, the aforementioned dimness of V_B[–] means that it has only been studied in ensembles and that high densities are required for bright emission.⁴⁷ Methods to enhance the brightness have been made primarily with Purcell enhancement via cavity engineering.^{48–50} However, such cavities and/or pillars degrade the facile integrability of the defect sensor into flat electronics.

We report that the emission intensity and overall sensitivity of the V_B[–] defect can be enhanced by simply adding another layer in a vdW heterostructure. Through experimentation at low temperatures, our findings reveal that both the absorption and photoluminescence characteristics of the V_B[–] defect are markedly improved when a lead(II) iodide (PbI₂) layer is present. This phenomenon is supported by a theoretical framework in which PbI₂ operates as a "photon ratchet," efficiently funnelling excitons towards the emitting hBN layer. The observed enhancement persists at room temperature and under conditions of low laser power, indicating the robustness of this approach across varying experimental

parameters. Moreover, we report an overall improvement in the defect's sensitivity to external environmental factors, as evidenced by continuous-wave optically detected magnetic resonance (cw-ODMR) measurements conducted with multiple excitation wavelengths. The optical response of the V_{B^-} defect to changes in an applied external magnetic field is presented as an example of this enhanced sensitivity.

In addition to these improvements in emission and sensitivity, our work provides, to the best of our knowledge, the first documented instance of defect emission enhancement achieved through energy transfer mechanisms. This represents a significant advancement in the engineering of spin-photon interfaces and the development of sensitive quantum sensors based on 2D materials.

1 RESULTS AND DISCUSSION

The results presented in this work were obtained from the exfoliation of a neutron-irradiated bulk crystal of hBN. The V_{B^-} color centers were generated in the bulk crystal via this neutron irradiation with a dose of $2.6 \times 10^{16} \text{ n cm}^{-2}$ as described previously³². The defects are assumed to be evenly distributed throughout the crystal. However, because the work concerns the enhancement of the dim PL of the V_{B^-} , to account for flake-to-flake variations in thickness and defect density, heterostructures were prepared with geometries that allowed analysis of isolated materials, with consistent hBN capping between regions. V_{B^-} emission was then compared for the same irradiated flake, with and without the donor layer. For clarity and ease, we will refer to normal hBN as “hBN” and neutron irradiated as “ V_{B^-} ”. In our case, we created a four-layer vdW heterostructure (as described in Methods): The top and bottom are native hBN capping layers, then the V_{B^-} layer, followed by a lead (II) iodide layer (PbI_2). An example structure is shown in **Figure 1a** and schematically rendered in **Figure 1d**.

The PbI_2 layer is considered the donor and sensitizer/antenna, increasing the absorption and emission from the acceptor, V_{B^-} in hBN. Emission from the PbI_2 free exciton (FE) is expected around 510 nm, while broad emission from the V_{B^-} defect is expected from 750 to 850 nm. Energy transfer in the four-layer heterostructures is demonstrated by heat maps of the PbI_2 free exciton and V_{B^-} emission intensities derived from spatially resolved spectra acquired from two subsequent scans, centring the grating on low-energy and high-energy regions. The mapped heterostructure region is outlined by white dashed lines in the white-light image (**Figure 1a**). Clear evidence of energy transfer from the PbI_2 FE to the V_{B^-} state is observed, manifested as donor quenching and acceptor enhancement. Specifically, a pronounced reduction in FE emission is evident in the overlapping region of the heterostructure (**Figure 1b**), accompanied by a concurrent enhancement of V_{B^-} emission localized to the same region (**Figure 1c**). Characteristic spectra from different regions of the heterostructure (**Figure 1e**), also demonstrate what we observe in the heat map that the FE of PbI_2 : the FE decreases in intensity in the coupled PbI_2 - V_{B^-} heterostructure (blue) compared to the capped PbI_2 region (green) while the V_{B^-} peak intensity increases in the heterostructure compared to the capped but uncoupled V_{B^-} flake (red).

Indications of the presence of structural inhomogeneities can be observed in the high-resolution TEM image of a multilayer PbI_2 flake (**Figure 1f**). These structural inhomogeneities result in the broad PL peak from 650 to 750 nm observed in the PbI_2 individual spectrum (and therefore also in the heterostructure spectrum), referred to as the PbI_2 self-trapped exciton (STE). Evidence of the STE in PbI_2 will be discussed further later in the text, but the long tails of this STE overlap with the V_{B^-} peak. Thus, to avoid overestimating the enhancement of the defect by the heterostructure, we calculated the enhancement factor using differential intensities, as shown in **Figure 1g**. The V_{B^-} spectrum is shown with the background spectrum subtracted, while the heterostructure spectrum is shown with the PbI_2

spectrum subtracted. The spectra are plotted on different scales so that both peaks are visible despite their different scales. Comparing these two returns in an overall defect signal enhancement of 45x in the coupled structure compared to the uncoupled V_{B^-} peak, and confirming the efficacy of our heterostructure.

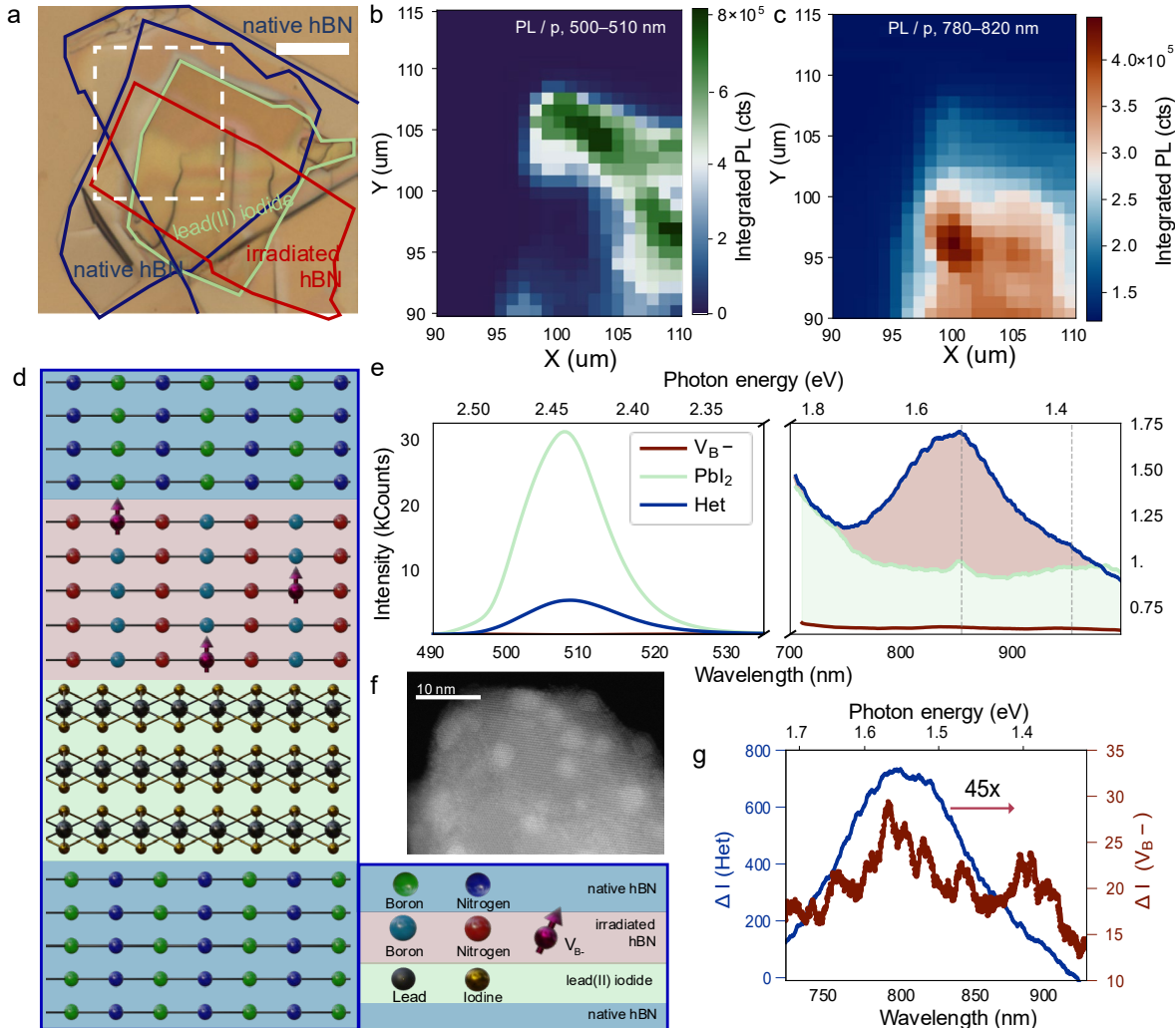


Figure 1 Enhanced defect emission in hBN–PbI₂ heterostructures at 4 K: **a)** White-light image of a four-layer van der Waals (vdW) heterostructure. In this structure, the top and bottom layers consist of native hBN, serving as capping layers and marked in dark blue. Immediately beneath the top hBN cap is the neutron-irradiated hBN layer containing negatively charged boron vacancies (V_{B^-}), marked in red. This is followed by PbI₂, outlined in light green. The area indicated by white dashed lines corresponds to the region that was mapped at a temperature of 4 kelvin. **b)** The PL intensity map displays the signal associated with the free exciton (FE) peak of PbI₂, at a wavelength range 500–510 nm ($\approx 505 \pm 5$ nm). **c)** The PL intensity map for the V_{B^-} defect peak was measured at a range of 780–820 nm ($\approx 800 \pm 20$ nm). **d)** A rendered schematic of the heterostructure. The rendering includes a key for atom types, with boron and nitrogen atoms in neutron-irradiated and native hBN, depicted in distinct colours for clarity in neutron-irradiated and native hBN. **e)** PL spectra corresponding to the regions identified in panels b) and c) are plotted. PbI₂ displays a pronounced FE peak and a STE peak. **f)** High-resolution transmission electron microscopy (TEM) shows the structural characteristics of PbI₂ at the atomic scale. **g)** Differential intensity analysis of the spectra shown in panel e). The background spectrum was subtracted from the V_{B^-} spectrum, and the PbI₂ spectrum from the heterostructure spectrum, yielding an enhancement factor of 45x for the low-temperature scan.

The low quantum efficiency of the negatively charged boron vacancy is understood by the dipole-forbidden transition between the ground state (GS) and excited state (ES) triplet manifolds in the absence of strain or electric fields⁴². The present work does not seek to modify the intrinsic emission process of the defect, but rather to introduce alternative pathways for optical absorption. In the heterostructure, the electronic structure and optical transition matrix elements differ from those of the individual materials, leading to modified absorption and emission characteristics. Importantly, the coupled system supports optical processes that involve photonic states from both materials. Under laser excitation, PbI_2 can absorb photons over a range of energies. One representative pathway, illustrated in **Figure 2a**, proceeds as follows: PbI_2 absorbs a photon of energy ω_1 and subsequently emits a lower-energy infrared photon ω_2 . The remaining energy excites the V_{B}^- defect, which then emits at its characteristic transition energy, $\Omega = \omega_1 - \omega_2$. In this way, a single high-energy photon is effectively converted into two lower-energy excitons—an infrared photon and a photon emitted by the defect. This process arises from the system's second-order nonlinear optical response. The second-order polarization, P , at frequency, Ω , can be expressed as the product of the second-order susceptibility tensor $\chi^{(2)}$ and the interacting electromagnetic fields, $E(\omega_1)$ laser field and $E(\omega_2)$ infrared photon field:

$$P^{(2)}(-\Omega) = \sum_{j,k} \chi_{ijk}^{(2)}(-\Omega; \omega_1, -\omega_2) E_j(\omega_1) E_k^*(\omega_2) \quad 1)$$

In the present treatment, we consider only this dominant two-photon nonlinear pathway, which is expected to be the fastest radiative channel. Phonon-assisted processes and higher-order multiphoton mechanisms are not included. The nonlinear polarization, in turn, governs the V_{B}^- emission intensity, I , which scales with its magnitude squared.

$$I(\Omega) \propto |P^{(2)}(\Omega)|^2 \quad 2)$$

Ab initio DFT details and calculations are provided in the Supplementary Information Section 1. The calculated spin density distribution around the defect is shown in **Figure 2b** and is consistent with previous theoretical studies.³⁰ The supercells used in the DFT calculations for an isolated V_{B}^- defect in hBN and for PbI_2 -stacked are presented in SI Figure 1. The results indicate negligible electronic hybridization between the defect and PbI_2 states. Consequently, the intrinsic radiative and nonradiative pathways of the spin defect remain largely unaffected, preserving its functionality as a spin qubit. Band structure and hybridized structure will be discussed later in the text (**Figure 3d**). Highly simplified modeling based on a 7×7 spin Hamiltonian is presented in Supplementary Section 4, where changes in eigenstate composition and basis-state mixing are calculated before and after PbI_2 coupling.

Increased absorption by the heterostructure for energies below the PbI_2 band gap was also observed, indicating PbI_2 exciton line renormalization in the presence of the irradiated hBN, as discussed previously for other 2D materials.^{51,52} In the differential reflectance scan in **Figure 2c**, which was performed for 550–555 nm at 4K, the heterostructure region shows a lower differential reflectance (blue) than either the PbI_2 or V_{B}^- layers alone. In **Figure 2d**, the theoretical absorption by the defect, when uncoupled, is compared with the defect absorption, when coupled with PbI_2 , for energies below the V_{B}^- emission wavelength. Absorption increases for all wavelengths below the emission energy of V_{B}^- , with a pronounced boost for excitation energies higher than the PbI_2 bandgap.

Emission enhancement was also predicted theoretically (Equation 2) and was estimated to be around one order of magnitude for most laser excitation wavelengths, consistent with the experimentally observed enhancement, ranging from 5 to 45x. The photoluminescent excitation (PLE) spectrum was taken in the heterostructure region using a supercontinuum laser, keeping the excitation power constant. The PLE data also shows increased defect emission (emission collected using a 775 LP filter) when

exciting with energies lower than the PbI_2 bandgap (SI Figure 3), supporting the supposition that PbI_2 exciton renormalization occurs near the irradiated hBN.

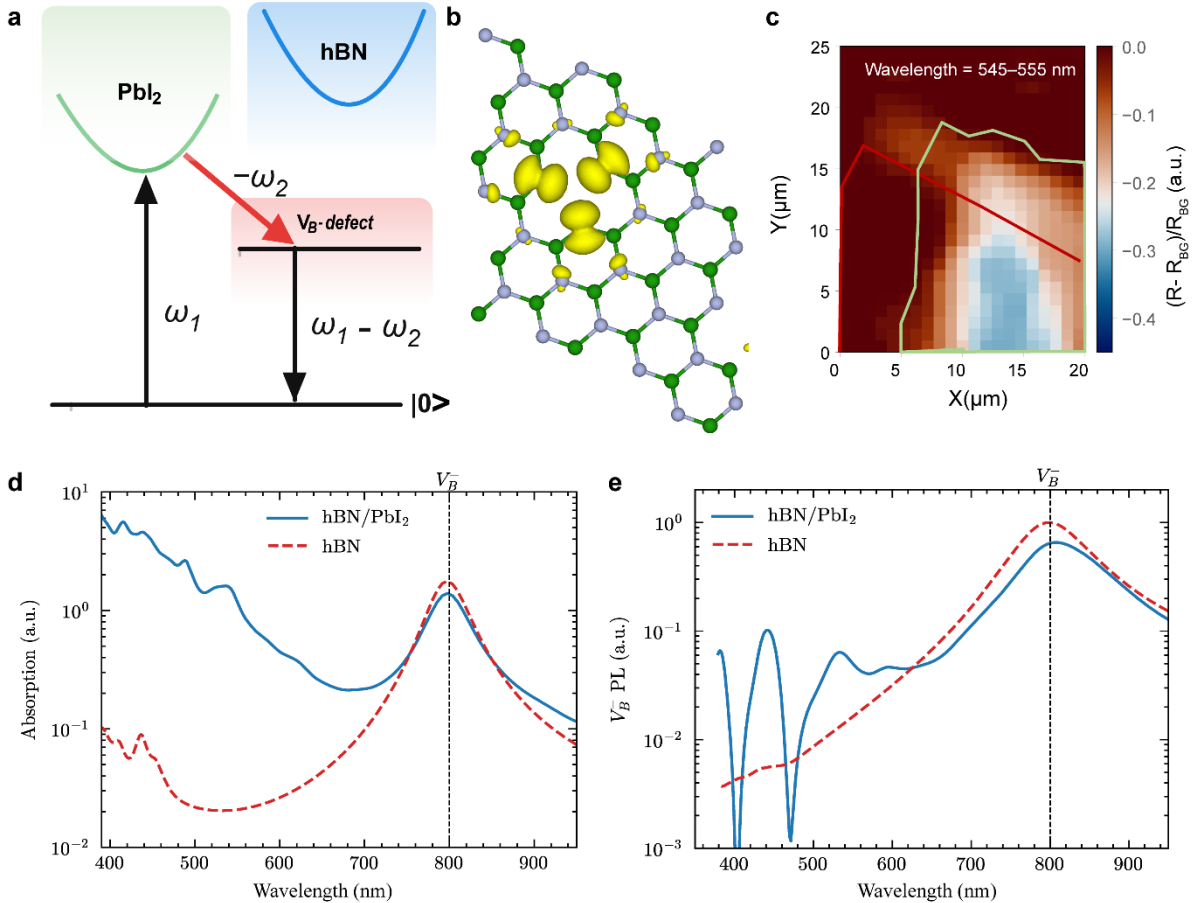


Figure 2 Energy-transfer mechanism and predicted optical response of $V_{\text{B}}\text{-}$ defects. **a)** Schematic of the energy-transfer process responsible for the emission enhancement, showing coupling between PbI_2 and the $V_{\text{B}}\text{-}$ defect in hBN. **b)** Spin density surrounding the vacancy. **c)** Differential reflectance (absorption) observed at 4K from the heterostructure in Figure 1. The coupling between PbI_2 (green outline) and $V_{\text{B}}\text{-}$ (red outline) increases absorption, even above the PbI_2 bandgap. **d)** Expected absorption of the defect when it's alone (red dashed) and coupled with lead iodide (blue) modeled by DFT. Absorption can be observed to increase in the coupled structure for energy below the emission energy of the defect, which is demarcated with a vertical dashed black line. **e)** Theoretical PL intensity of the uncoupled defect (green dashed) and $\text{PbI}_2\text{-}V_{\text{B}}\text{-}$ coupled structure (blue). The emission energy line of the defect is again demarcated with a vertical dashed black line

After confirming enhanced absorption and photoluminescence in the coupled structure both theoretically and at low temperature, we assessed performance at room temperature to evaluate suitability for practical sensing under ambient conditions. We observed clearly the same characteristic quenching of the donor (PbI_2) and enhancement of the acceptor ($V_{\text{B}}\text{-}$) in our heterostructure at RT (Figure 3a-c) as observed at 4K (Figure 1a-c). Overall, we observed an enhancement range of 4 to 18x at room temperature, determined in the same manner as described for Figure 1 at room temperature. The differential spectra are shown in SI Figure 4 for the room temperature PL shown in Figure 3. The confocal measurements of PL spectra are described in *Methods*, and another example heterostructure that was examined at room temperature is shown in SI Figure 5.

Energy transfer (ET) was approached via two pathways: Type I band alignment and Fluorescence Resonance Energy Transfer (FRET). PbI_2 was selected as the donor material owing to its

favourable bandgap (2.4 eV) and band alignment with the V_{B^-} “bandgap” within the wide bandgap of hBN and its layered crystal structure, which can be mechanically exfoliated and readily integrated into vdW heterostructures.^{53,54} Transition metal dichalcogenides (TMDs) were also considered but the band gaps often fall within the range of 1.0–2.0 eV, which is the red to near infrared regions and currently, which does not satisfy the demands for the blue to UV emission. Alternatively, PbI_2 emits in the green-blue spectrum and has high absorption (approaches 10^5 cm^{-1}),^{55,56} making it an attractive donor material. It also exhibits interesting optical properties, such as photon upconversion⁵⁷ and ultrafast saturable absorption⁵⁸.

While the size and vacuum-level position of the PbI_2 bandgap are relatively well established, the V_{B^-} “bandgap” has been inferred theoretically from previous studies.^{59,60,30} The electronic bands of the two materials recovered by DFT can be observed in **Figure 3d**. The PbI_2 valence band is well below the highest occupied orbital of the defect, such that the electron will travel to a lower energy state when migrating from PbI_2 to the V_{B^-} state in hBN. On the other hand, the conduction band states are close in energy for the two materials, with the conduction band of PbI_2 slightly lower than that of the defect. This can indicate that the exciton does not effectively migrate. However, based on the accepted errors of DFT energy calculations and experimental results showing otherwise, this small energy hill can be accepted to allow exciton migration from PbI_2 to V_{B^-} , characteristic of Type I band alignment. A simplified diagram for this process is shown in **Figure 3e** where the numbers around the gaps are energy from vacuum for the valence and conduction bands for each material, as placed around the Fermi levels established by Kelvin Probe Force Microscopy (KPFM) in **Figure 3f**.

Fermi levels of the three heterostructure materials, as well as their slight variations due to stacking, were probed experimentally via KPFM, performed in vacuum. KPFM probes the Fermi level from vacuum. In our structure, it varies by material but remains in a 0.5 eV range, enabling the energy transfer discussed. The area off of the structure is gold, and its Fermi level is 5.1 eV from vacuum. The KPFM measurement procedure and calibration are detailed in *Methods*. To determine the effect of band-bending during stacking, the structure fabricated for KPFM has areas where one, two, and three layers exist. The results indicate, as predicted from this work and previous theoretical works,^{59,30} that the Fermi levels of the materials are well aligned to promote energy transfer via exciton migration, given the band gap sizes well established by optical measurements for PbI_2 and predicted by theory for V_{B^-} . FRET is also available in the coupled structure, supported by the experimental emission and absorption spectrum in **Figure 3g**. Absorption spectra were recorded using a bulk neutron-irradiated hBN crystal.

Finally, the lifetime of the defect was recorded in the heterostructure as well as the bare V_{B^-} , exciting with a 555 nm laser (**Figure 3h**). A 775 nm long-pass (LP) filter was used to filter out the emission from the STE in PbI_2 . The lifetime of the defect is observed to be shorter in the heterostructure, which is likely due to the increased spin-orbit coupling and intersystem crossing--due to the presence of heavy atoms lead and iodine-- as well as a small Purcell effect due to the difference in refractive index. The lifetime of the defect at 4K on and off the heterostructure was also measured using an excitation of 460 nm, this time energetically higher than the PbI_2 bandgap. This data was also recorded with a 775 nm LP filter and reports the same lifetime shortening phenomena (SI Figure 6). The lifetime of the heterostructure and the PbI_2 is also reported in SI Figure 6, indicating donor lifetime shortening through energy transfer but too small to be conclusive. Although the data here is normalized, enhanced

emission is still observed upon excitation below the PbI_2 bandgap, as predicted by theory (Figure 2e)

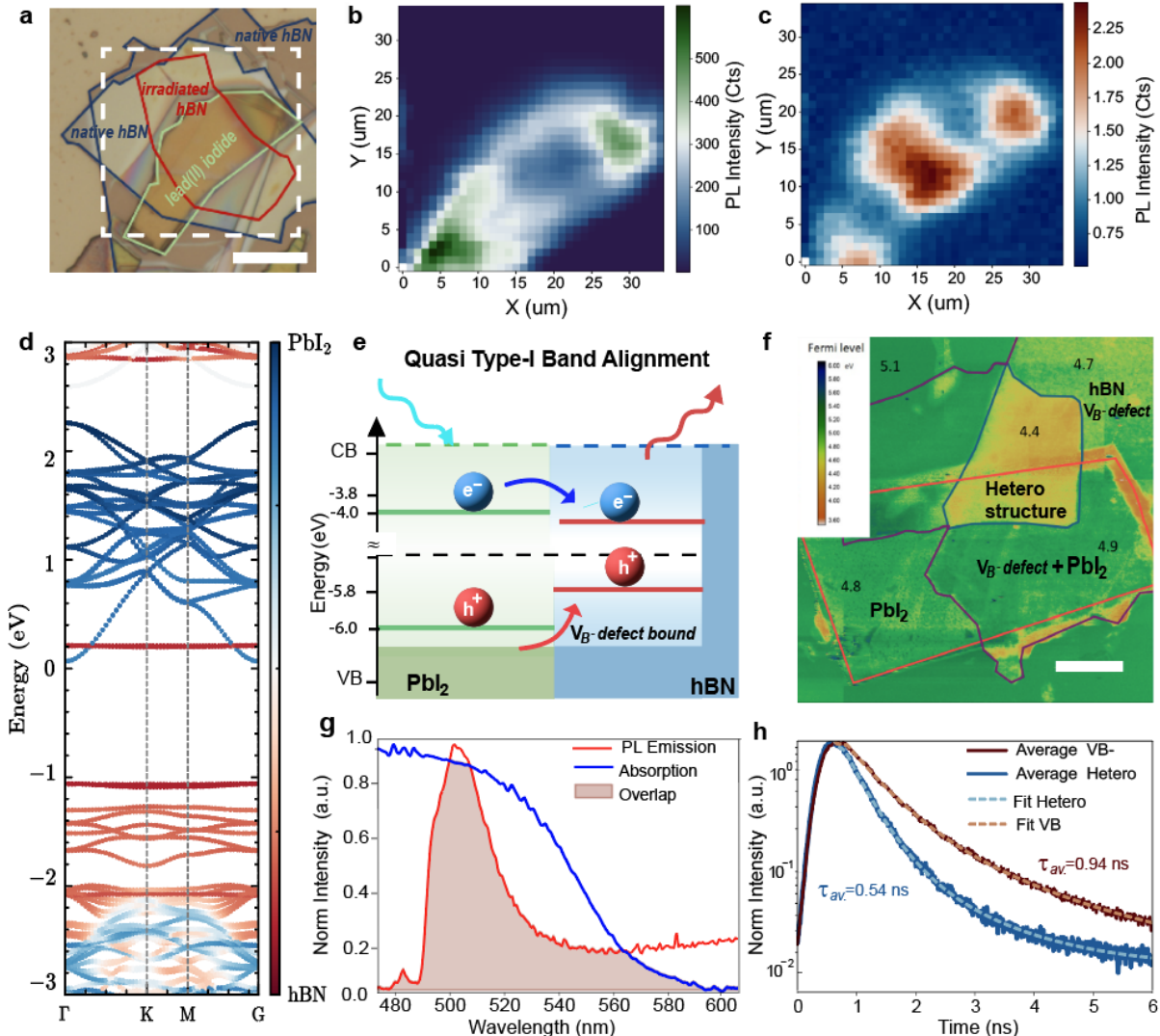


Figure 3 Room temperature heterostructure response: **a)** A white-light image of the imaged four-layer vdW heterostructure. The top and bottom layers consist of native hBN flakes serving as capping layers and marked in dark blue. Beneath the top hBN is the neutron-irradiated hBN layer (V_{B}^-), marked in red. This is followed by PbI_2 , outlined in light green. The area in white dashed lines was mapped at RT. **b)** The PL intensity map of the signal associated with the free exciton peak of PbI_2 , $510 \pm 10 \text{ nm}$. **c)** The PL intensity map for the V_{B}^- , detected at $800 \pm 20 \text{ nm}$. **d)** DFT calculated band diagram for PbI_2 (blue) and V_{B}^- in hBN (red), where white would be completely hybridized. **e)** Simplified rendering of type I (straddling) band alignment, where the band gaps size are based on theory and centered around the Fermi levels determined by KPFM. **f)** Kelvin probe force microscopy (KPFM) of overlapping layers of PbI_2 (bottom, red), V_{B}^- (purple, middle), and hBN (blue, top). **g)** Emission and absorption overlap integral required for FRET. Emission of PbI_2 is in red and absorption of neutron-irradiated hBN is in blue. **h)** Lifetimes of the coupled (red) vs uncoupled (blue, labeling is currently wrong) structures. The lifetime of the heterostructure is observed to be lower. Both are fit via biexponential decay curves.

To investigate the recombination mechanisms of various excitons present within the heterostructure, a detailed power analysis was conducted on the relevant regions. The power ranged from $1.5 \mu\text{W}$ to $16 \mu\text{W}$. The confocal scans were done with a one μm laser spot (power density 1.91 kW cm^{-2} to 20.4 kW cm^{-2}). Excitation and acquisition parameters were chosen to maintain defect signal visibility while avoiding saturation of the PbI_2 free-exciton emission. In the PbI_2 region, two primary excitonic features are observed (Figure 4a): the free exciton (FE) and the broad emission feature

spanning 600 to 750 nm, the self-trapped exciton (STE). The STE arises when an exciton becomes localized due to a distortion in the crystal lattice,⁶² a phenomenon that is also linked to the presence of iodine vacancies.⁶³ This localization significantly redshifts the emission energy, resulting in a broad spectral feature that reflects transitions between multiple vibronic bands. The STE mechanism is schematically depicted in SI Figure 7, with further discussion on irradiation-induced inhomogeneities following. To investigate the STE and structural inhomogeneities, we performed high-resolution TEM and element analysis TEM (**Figures 4b** and **4c**, respectively). The TEM images indicate the structural inhomogeneities observed in the PL. There are regions of thinner and thicker layers, as well as regions of lead buildup, consistent with the previous prediction that the STE emission in the orange-red region was to be associated with iodine vacancies.⁶³

In the heterostructure, the emission of the FE, STE and V_{B^-} are observed to increase with increasing excitation power (**Figure 4c**). The differential intensity (het-PbI₂, as discussed in **Figure 1e**) as a function of laser power is also shown in the inset. As the laser power increases, the V_{B^-} emission becomes more prominent. The neutron irradiated region PL vs power is shown in SI Figure 8, showing that the V_{B^-} peak also increases as a function of laser excitation power, but at a slower rate and lower overall intensity than in the heterostructure.

Figure 4f presents power-dependent emission spectra from the PbI₂–hBN heterostructure, showing a continuous increase in V_{B^-} defect emission with increasing excitation fluence. The absence of roll-off indicates that the defect ensemble remains far from saturation within the measured power range. Power-law analysis yields similar scaling exponents for coupled and uncoupled regions, indicating that PbI₂ does not alter the intrinsic radiative efficiency of the defect ensemble, but rather enhances the effective excitation experienced by V_{B^-} centers, as predicted by our energy transfer mechanism. Correspondingly, the V_{B^-} peak intensity increases approximately 33× faster (with 9increasing power) in the heterostructure than in neutron-irradiated hBN alone (Supplementary Fig. 8). Peak intensities were extracted using two-Gaussian fits for heterostructure spectra and single-Gaussian fits for neutron-irradiated regions (Supplementary Fig. 8).

Figure 4e quantifies ensemble-level coupling by plotting the change in V_{B^-} emission intensity against baseline defect photoluminescence. The observed linear scaling demonstrates that PbI₂-induced enhancement is proportional to the intrinsic defect emission strength, consistent with increasing ET events energy transfer rather than defect saturation. Given the effectively unlimited PbI₂ exciton reservoir, this behaviour supports a transfer-limited regime, in which a substantial fraction of donor excitons recombine through competing pathways, consistent with the persistence of PbI₂ FE and STE emission peaks observed in the coupled structure spectrum.

Temperature-dependent PL (**Figure 4g**) reveals a multi-order-of-magnitude increase in PbI₂ FE emission upon cooling, accompanied by a commensurate enhancement of V_{B^-} defect luminescence in the heterostructure. This indicates that improved donor exciton efficiency strengthens defect sensitization, suggesting additional performance gains at low temperature.

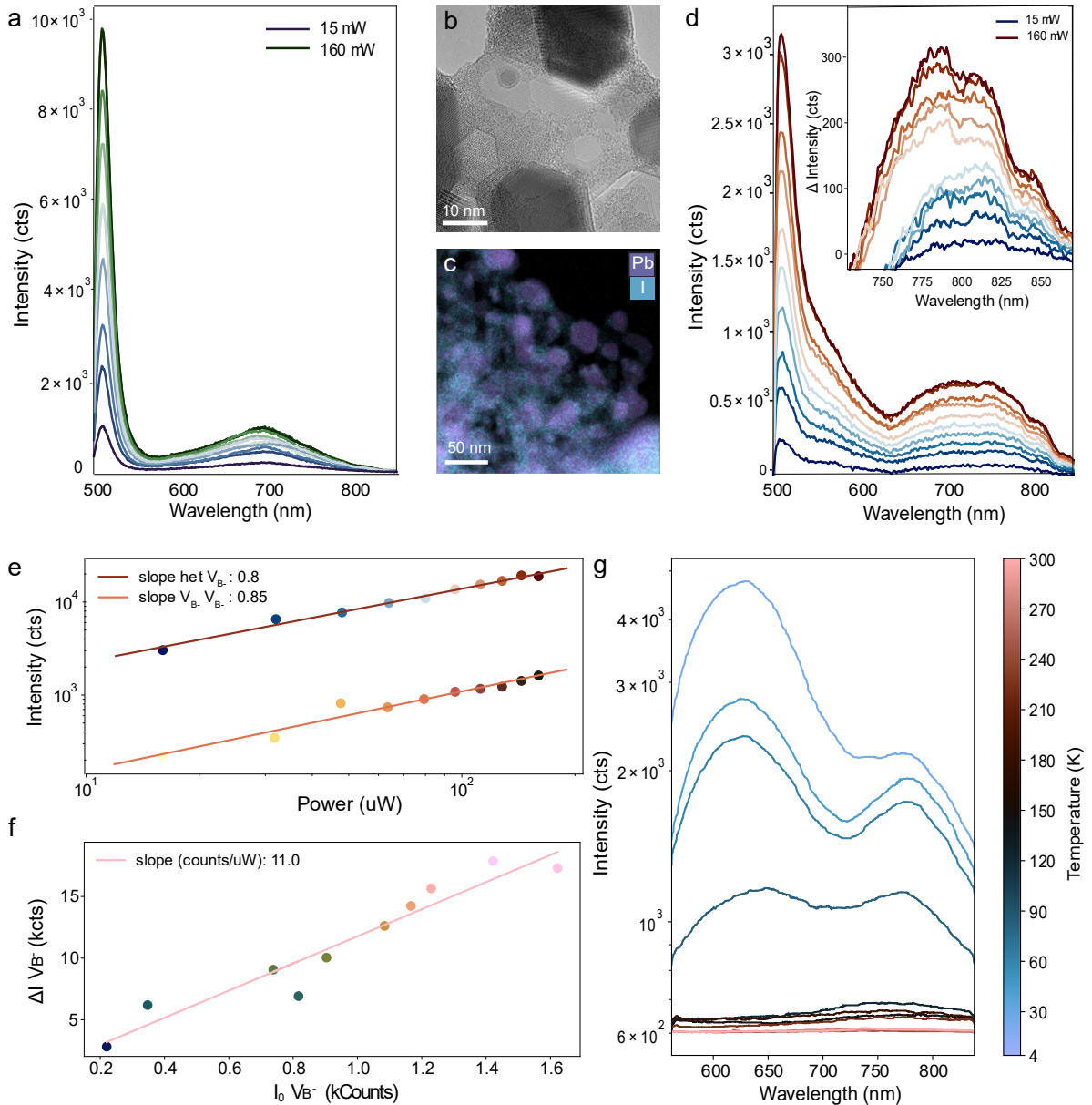


Figure 4 Emission Characteristics: **a)** PL versus power for the PbI_2 (capped with hBN) region of heterostructure, referred to as PbI_2 . The background (off-heterostructure) was subtracted. The power scales from 15 μW to 160 μW over a 1 μm point (power density 1.91 kW cm^{-2} to 20.4 kW cm^{-2}). **b)** High-resolution TEM of a PbI_2 flake is shown, demonstrating local structural inhomogeneities. The scale bar is 10 nm. **c)** Element analysis TEM (EDX) of a PbI_2 flake. is shown in purple. Iodine is shown in blue. The scale bar is 50 nm. Regions of lead buildup can be observed. **d)** PL versus power for the heterostructure region (all four layers). Background is subtracted. The inset shows the differential heterostructure PL, where differential PL is defined as the PL from PbI_2 region subtracted from the all-layer heterostructure region. Subtracting the STE recovers the PL from the defect. **e)** Power plot of the intensities of the V_{B}^- peak in heterostructure vs in neutron-irradiated hBN. **f)** Difference between V_{B}^- ensemble emission coupled and uncoupled to a PbI_2 donor layer, plotted against the baseline uncoupled defect luminescence. **g)** PL intensity of the low-energy defect spectral region versus temperature.

The V_{B}^- defect is primarily of interest as a qubit platform, here as a sensor. The V_{B}^- electron spin can be off-resonantly excited from its spin-triplet ground state to its spin-triplet excited state via optical absorption/laser irradiation. Because the non-radiative, spin flip decay channel (accessed via

intersystem crossing) preferentially couples to the $m_s = \pm 1$ sublevels of the excited states, excitation of the $m_s = \pm 1$ states results in lower PL. A simplified energy diagram for the V_{B^-} qubit is shown in **Figure 5a**, where D_{gs} is the room-temperature natural ground-state splitting between sublevels $|0\rangle$ and $|\pm 1\rangle$ and D_{es} is the room-temperature natural excited-state splitting between sublevels $|0\rangle$ and $|\pm 1\rangle$. This difference in PL enables one to read out the electron spin state and is known as the contrast.

Optically detected magnetic resonance (ODMR) is used here to probe these states. In ODMR, the PL is monitored while sweeping the frequency of the microwave delivered to the sample via an antenna. The setup is illustrated schematically in **Figure 5b**, and ODMR methods are further described in *Methods*. When the frequency crosses a transition where the energy is equivalent to the energy between the ground state electron spin sublevels, the resonance is evidenced as a drop in the PL signal.

$$\nu_{1,2} = \frac{D_{gs}}{h} \pm \frac{1}{h} * \sqrt{E_{gs}^2 + (g\mu_B B)^2} \quad 3)$$

The full form of the resonant features, including an external magnetic field, is described by Equation 3: D_{gs} and E_{gs} denote the ground state longitudinal and transverse zero-field splitting parameters, respectively. h is Planck's constant. μ_B is the Bohr magneton, and g is the Landé factor (2,000). From this work, we derive $D_{gs}/h = 3.46$ GHz and $E_{gs}/h = 55 \pm 5$ MHz, which is in good agreement with previous works on the V_{B^-} .^{32,64}

In our case, the PL counts were recorded as a function of microwave frequency, comparing different regions of the heterostructure. The system is excited off-resonantly by either a 488 nm (**Figure 5c**) or 555 nm (**Figure 5d**) laser, and, in both cases, we observe a strong improvement of the PL signal in the heterostructure region while retaining the same resonant features as the V_{B^-} region. As can be observed in Equation 3, the difference in energy between the $m_s = \pm 1$ sublevels can be altered by a magnetic field, B . The variance of the resonant features of the ODMR spectrum of the defect as a function of the magnetic field is shown in **Figures 5e** and **5g**.

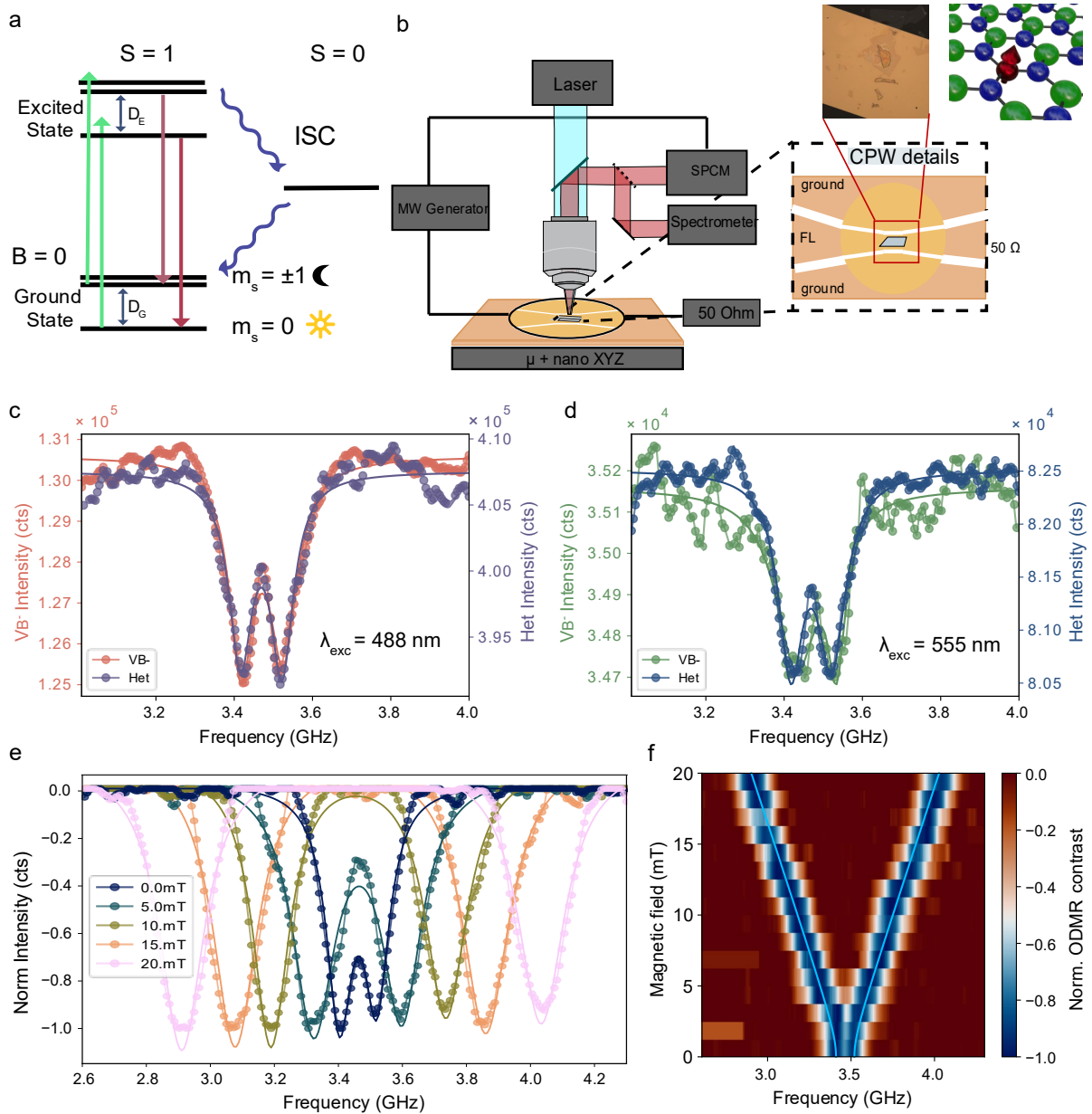


Figure 5 ODMR and Sensing Magnetic Fields: **a)** Energy level diagram for V_{B}^- and schematic illustration of the readout by ODMR. The system was excited off-resonantly via a laser (green arrow). ODMR contrast is governed by differing rates of radiative decay (red arrows) vs nonradiative decay via intersystem crossing (ISC, purple arrow) to the meta-stable (MS) singlet state from the excited state to ground state. Dips in photoluminescence are observed at the frequency corresponding to the energy difference between $m_s = 0$ and $m_s = \pm 1$ (D_{gs}). **b)** Schematic illustration of the ODMR setup. A coplanar waveguide (CPW) is placed in the center of the path with the heterostructure placed onto the feedline (antenna). This CPW is wire-bonded to a PCB, which interfaces with the signal generator (SG) and 50 Ohm impedance termination. The sample is excited using a laser, and emission is detected by the APD, which is triggered by the change in frequency from the SG. **c)** ODMR spectra when the V_{B}^- (left, pink) vs the heterostructure (right, purple) are excited by a 488 nm laser. **d)** ODMR spectra when the V_{B}^- (left, green) vs the heterostructure (right, blue) are excited by a 555 nm laser. **e)** Normalized ODMR of the heterostructure with varying magnetic fields. **f)** Points from e, as well as additional points, are plotted as the magnetic field versus resonance frequency.

To probe the sensing capability of the defect, we applied an external magnetic field and measured the corresponding shift in the resonant ODMR peaks. Selected datapoints are plotted on a

normalized scale in **Figure 5e**, showing the expected characteristics: As the magnetic field increases, the separation of the resonance peaks increases. Peaks are shown with their full contrast (non-0-1 scale) in SI Figure 9. Various magnetic fields vs the resonance frequency were then plotted as a heat map (**Figure 5f**), demonstrating the ability to sense the field using the resonance position of ODMR peaks. The theoretical resonance frequencies (Equation 3) vs the magnetic field are plotted in light blue and clearly agree with the experimental results.

$$\eta_{CW} = \frac{4}{3 * \sqrt{3}} \frac{h}{g_e \mu_B} \frac{\Delta\nu}{\gamma_e C_{CW} \sqrt{R}} \quad 4)$$

To quantify the impact of the PbI_2 ratcheting layer on V_{B^-} utility, we evaluated the continuous-wave ODMR (cw-ODMR) sensitivity. As defined in Equation 4, sensitivity depends on the ODMR linewidth ($\Delta\nu$), contrast (C_{CW}), and photoluminescence count rate (R). γ_e is the gyromagnetic ratio of an electron. All measurements were performed at room temperature; to minimize PbI_2 STE emission, a 775 nm LP filter was used. Because a substantial fraction of V_{B^-} emission lies below this cutoff (Supplementary Figure 8), the reported enhancement represents a conservative lower bound. Under 488 nm excitation, the heterostructure exhibits a 4 \times increase in PL counts while preserving resonance positions (Fig. 5c); under 555 nm excitation, a 3 \times increase is observed (Fig. 5d). This photon-collection gain, with moderate changes to contrast, results in a 190% sensitivity improvement at 488 nm and a 325% improvement at 555 nm (Supplementary Tables 1–2). The best-performing heterostructure achieves a sensitivity of $76 \mu\text{T Hz}^{-1/2}$ at $160 \mu\text{W}$, representing an approximately threefold improvement over the previously reported optimized V_{B^-} sensitivity at comparable power.⁶⁵ Notably, the sensitivity advantage grows at lower excitation powers, reaching an improvement of $\sim 350 \mu\text{T Hz}^{-1/2}$ at $16 \mu\text{W}$ with 488 nm excitation (Supplementary Fig. 10). Given the short-range nature of the donor–defect photon and energy transfer ($\sim 10 \text{ nm}$) and the enhanced radiative efficiency at low temperature, further gains are expected in thinner neutron-irradiated flakes and under cryogenic operation, which should be explored in future work.

2 CONCLUSION

Through the use of a sensitizing donor layer in a van der Waals heterostructure, this work demonstrates that the photoluminescence yield and sensing performance of a quantum defect sensor, here, the V_{B^-} in hBN, can be substantially enhanced. Beyond improving emission yield, this work establishes a proof-of-concept for enhancing defect emission via interlayer coupling in vdW heterostructures, unlocking a methodology that can be fine-tuned and applied to other systems. A photonic ratchet mechanism yields a two-orders-of-magnitude enhancement in defect emission at 4 kelvin and retains an order-of-magnitude enhancement at room temperature, and ET is confirmed by reciprocal photoluminescence mapping showing concurrent suppression of PbI_2 free-exciton emission and amplification of V_{B^-} defect luminescence. Complementary DFT calculations, together with absorption and photoluminescence spectroscopy, indicate enhanced optical absorption and emission in the coupled heterostructure, consistent with efficient donor-to-defect energy transfer. Finally, continuous-wave ODMR measurements demonstrate substantial sensitivity gains across multiple excitation wavelengths at room temperature, underscoring the promise of this platform for scalable quantum sensing of external magnetic fields.

3 METHODS

3.1 Heterostructure Fabrication

Commercially available hBN bulk crystals (HQ Graphene) were neutron irradiated at facilities at OSU to generate V_B defects, as previously described³². The heterostructure was fabricated by a dry-transfer technique using polycarbonate (PC) membranes. Individual flakes were mechanically exfoliated onto SiO_2/Si substrate with oxide thickness of 270 nm using the cleavage technique method pioneered for the production of graphene⁶⁶. The same mechanical exfoliation technique was used for PbI_2 and hBN that had not been neutron irradiated. The heterostructure was made by picking up the flakes successively using the PC stamp, and then releasing them onto ODMR antennas by increasing the temperature above 150 °C⁶⁷.

3.2 Confocal Microscopy

The PL properties were analysed with a home-built scanning confocal microscope operating at ambient conditions. A laser excitation at 405 nm, 488 nm, or 555 nm (Omicron BrixXHub-6) was focused onto the sample with a high numerical aperture microscope objective (NA = 0.95) mounted on a three-axis MCL Nanodrive piezoelectric scanner (MCLC02485) and an MCL Microdrive (MCL-microD2035). A 4f imaging configuration was used before directing the excitation to the sample via the appropriate long-pass dichroic mirror. The PL signal was collected by the same objective, filtered via a long pass filter with wavelength depending on the application, and focused on to a 50-μm-diameter pinhole, and finally directed either to a spectrometer (Ocean Optics QEPro High Performance Spectrometer) or to a silicon avalanche photodiode operating in the single-photon counting regime (PerkinElmer Optoelectronics Photon Counting Module, Model: SPCM-AQR-14-FC). Single-point spectra, ODRM, or x-y PL scans were performed. The lateral spatial resolution of the microscopy was around 1 μm.

3.3 Optically Detected Magnetic Resonance

Optically detected magnetic resonance (ODMR) spectra were recorded by monitoring the PL signal while sweeping the frequency of a microwave field applied through a gold coplanar waveguide (antenna) onto which the heterostructure was transferred. The gold antenna was patterned on the coverslip using photolithography and electron beam evaporation of 5 nm titanium and 50 nm gold. The antenna was then wire bonded to a copper coplanar waveguide printed circuit board (PCB) that interfaces with the signal generator (Siglent SSG5060X-V) interfaced with a copper waveguide PCB to the sample surface. When the microwave frequency crosses a transition where the energy is equivalent to the energy between the ground state electron spin sublevels, the magnetic resonance is evidenced as a drop of the PL signal. At zero external magnetic field, the resonance frequencies are given by $\nu_{\pm} = D \pm E$, where D and E denote the longitudinal and transverse zero-field splitting parameters, respectively. The external magnetic field was achieved with a NdFeB magnet (N35) that was positioned above the sample stage and could be raised and lowered with a Z-axis positioner.

3.4 Kelvin Probe Force Microscopy

Kelvin probe force microscopy⁶⁸ (KPFM) measurements on the 2D heterostructures were performed using a tip-scanning atomic-force microscope (AFM) inside a scanning electron microscope (SEM).⁶⁹ Self-sensing, piezo-resistive polymer AFM cantilevers⁷⁰ were used to eliminate optical laser beam-induced effects on surface potential and enable measurements in a compact in-vacuum environment. The cantilever deflection was read out via the integrated piezo-resistive bridge circuits

and used for topography feedback in amplitude-modulation AFM mode. KPFM was implemented in a heterodyne configuration:⁷¹ an AC bias V_{ac} was applied between tip and sample at a frequency f_{el} chosen such that the resulting electrostatic force detection is at the second eigen mode $f_2 = f_1 + f_{el}$, f_1 being the first eigen mode of the cantilever and the mechanical carrier frequency. The KPFM feedback loop nulled the electrostatic interaction by adjusting the DC bias V_{dc} until the electrostatic response was minimized, and the resulting compensating bias was recorded as the contact potential difference (CPD) map alongside topography in a single pass.

To avoid beam-induced contamination and work-function drift, the specimen was not exposed to the SEM electron beam until completion of all KPFM acquisitions; SEM imaging was performed only afterwards for navigation. To reference the work function, the 2D material flakes were prepared on an evaporated Au film that served as an internal reference region within each scan. The large-area CPD map was generated by acquiring a tiled dataset (10 partially overlapping frames of 20 μm x 20 μm) under identical KPFM parameters, aligned using overlap-based translation, and then stitched into a single mosaic. Residual offsets between tiles were corrected by enforcing consistent CPD values over the Au reference region in the overlaps. Fermi level values were calculated from CPD values using $CPD = (\phi_{tip} - \phi_{sample})/e$, where ϕ is the work function and e is the elementary charge. With the tip work function calibrated against Au as reference in each scan, we computed the referenced potential offset as $\Delta V(x, y) = V_{CPD}(x, y) - \langle V_{CPD} \rangle_{Au}$, where $\langle V_{CPD} \rangle_{Au}$ is the mean CPD measured for Au. The local sample work function was then obtained as $\phi_{sample}(x, y) = \phi_{Au} - \Delta V(x, y)$, assuming $\phi_{Au} = 5.1$ and the equivalence $1\text{V} = 1\text{eV}/e$. The Fermi levels relative to the vacuum level were reported as $E_F(x, y) = -\phi_{sample}(x, y)$.

4 ACKNOWLEDGMENTS

E.M. and A.R. would like to thank Dr Arianna Marchioro (LBP and EPFL) for the photochemical mechanism discussions and experimental advice and Dr David Reyes (CIME EPFL) for TEM imaging, analysis, and overall expertise on sample prep for difficult samples such as PbI₂. E.M and A.R. also would also like to thank CMI EPFL for the technical support and facilities. E.M and A.R. acknowledge support by the European Research Council (grant 101020445–2D-LIQUID). Y.Z. and O. V. Y. acknowledge support by the Swiss National Science Foundation (grant 224624).

5 REFERENCES

1. Vaidya, S., Gao, X., Dikshit, S., Aharonovich, I. & Li, T. Quantum sensing and imaging with spin defects in hexagonal boron nitride. *Adv. Phys. X* **8**, 2206049 (2023).
2. Togan, E. *et al.* Quantum entanglement between an optical photon and a solid-state spin qubit. *Nature* **466**, 730–734 (2010).
3. Pla, J. J. *et al.* High-fidelity readout and control of a nuclear spin qubit in silicon. *Nature* **496**, 334–338 (2013).
4. Awschalom, D. D., Hanson, R., Wrachtrup, J. & Zhou, B. B. Quantum technologies with optically interfaced solid-state spins. *Nat. Photonics* **12**, 516–527 (2018).
5. Wolfowicz, G. *et al.* Quantum guidelines for solid-state spin defects. *Nat. Rev. Mater.* **6**, 906–925 (2021).
6. Balasubramanian, G. *et al.* Nanoscale imaging magnetometry with diamond spins under ambient conditions. *Nature* **455**, 648–651 (2008).
7. Kucsko, G. *et al.* Nanometre-scale thermometry in a living cell. *Nature* **500**, 54–58 (2013).
8. Gao, X. *et al.* Single nuclear spin detection and control in a van der Waals material. *Nature* **643**, 943–949 (2025).
9. Pollok, S. *et al.* Magnetic microscopy for operando imaging of battery dynamics. *Nat. Commun.* **16**, 1–15 (2025).
10. Christle, D. J. *et al.* Isolated electron spins in silicon carbide with millisecond coherence times. *Nat. Mater.* **14**, 160–163 (2015).
11. Son, N. T. *et al.* Developing silicon carbide for quantum spintronics. *Appl. Phys. Lett.* **116**, 190501 (2020).

12. Castelletto, S. & Boretti, A. Silicon carbide color centers for quantum applications. *J. Phys. Photonics* **2**, 022001 (2020).
13. Robledo, L., Bernien, H., van Weperen, I. & Hanson, R. Control and Coherence of the Optical Transition of Single Nitrogen Vacancy Centers in Diamond. *Phys. Rev. Lett.* **105**, 177403 (2010).
14. Maurer, P. C. *et al.* Room-temperature quantum bit memory exceeding one second. *Science* **336**, 1283–1286 (2012).
15. Zvi, U. *et al.* Engineering spin coherence in core-shell diamond nanocrystals. *Proc. Natl. Acad. Sci.* **122**, e2422542122 (2025).
16. Kim, D. *et al.* A CMOS-integrated quantum sensor based on nitrogen–vacancy centres. *Nat. Electron.* **2**, 284–289 (2019).
17. Tisler, J. *et al.* Fluorescence and Spin Properties of Defects in Single Digit Nanodiamonds. *ACS Nano* **3**, 1959–1965 (2009).
18. Gardill, A., Cambria, M. C. & Kolkowitz, S. Fast Relaxation on Qutrit Transitions of Nitrogen-Vacancy Centers in Nanodiamonds. *Phys. Rev. Appl.* **13**, 034010 (2020).
19. Turunen, M. *et al.* Quantum photonics with layered 2D materials. *Nat. Rev. Phys.* **4**, 219–236 (2022).
20. Montblanch, A. R.-P., Barbone, M., Aharonovich, I., Atatüre, M. & Ferrari, A. C. Layered materials as a platform for quantum technologies. *Nat. Nanotechnol.* **18**, 555–571 (2023).
21. Dean, C. R. *et al.* Boron nitride substrates for high-quality graphene electronics. *Nat. Nanotechnol.* **5**, 722–726 (2010).
22. Dean, C. R. *et al.* Boron nitride substrates for high-quality graphene electronics. *Nat. Nanotechnol.* **5**, 722–726 (2010).
23. Jiang, S., Shan, J. & Mak, K. F. Electric-field switching of two-dimensional van der Waals magnets. *Nat. Mater.* **17**, 406–410 (2018).
24. Ciarrocchi, A. *et al.* Polarization switching and electrical control of interlayer excitons in two-dimensional van der Waals heterostructures. *Nat. Photonics* **13**, 131–136 (2019).
25. Cao, G. *et al.* 2D Material Based Synaptic Devices for Neuromorphic Computing. *Adv. Funct. Mater.* **31**, 2005443 (2021).

39. Udvarhelyi, P. *et al.* A planar defect spin sensor in a two-dimensional material susceptible to strain and electric fields. *Npj Comput. Mater.* **9**, 150 (2023).

40. Gong, R. *et al.* Coherent dynamics of strongly interacting electronic spin defects in hexagonal boron nitride. *Nat. Commun.* **14**, 3299 (2023).

41. Tárkányi, A. & Ivády, V. Understanding Decoherence of the Boron Vacancy Center in Hexagonal Boron Nitride. *Adv. Funct. Mater.* **n/a**, e11300.

42. Reimers, J. R. *et al.* Photoluminescence, photophysics, and photochemistry of the V_B defect in hexagonal boron nitride. *Phys. Rev. B* **102**, 144105 (2020).

43. Steiner, C. *et al.* Current-induced brightening of vacancy-related emitters in hexagonal boron nitride. *Phys. Rev. Res.* **7**, L032037 (2025).

44. Rizzato, R. *et al.* Extending the coherence of spin defects in hBN enables advanced qubit control and quantum sensing. *Nat. Commun.* **14**, 5089 (2023).

45. Qian, P. *et al.* Investigation of spin defects in hexagonal boron nitride generated via ion implantation. *Opt. Express* **32**, 46489–46499 (2024).

46. Zhou, H.-J. *et al.* Detection and manipulation of surface electric field noise of hexagonal boron nitride. Preprint at <https://doi.org/10.48550/arXiv.2506.07734> (2025).

47. Carbone, A. Quantifying the creation of negatively charged boron vacancies in He-ion irradiated hexagonal boron nitride. *Phys. Rev. Mater.* **9**, (2025).

48. Qian, C. *et al.* Unveiling the Zero-Phonon Line of the Boron Vacancy Center by Cavity-Enhanced Emission. *Nano Lett.* **22**, 5137–5142 (2022).

49. Xu, X. *et al.* Greatly Enhanced Emission from Spin Defects in Hexagonal Boron Nitride Enabled by a Low-Loss Plasmonic Nanocavity. *Nano Lett.* **23**, 25–33 (2023).

50. Sakib, M. A. *et al.* Purcell-Induced Bright Single Photon Emitters in Hexagonal Boron Nitride. *Nano Lett.* **24**, 12390–12397 (2024).

51. Raja, A. *et al.* Coulomb engineering of the bandgap and excitons in two-dimensional materials. *Nat. Commun.* **8**, 15251 (2017).

52. Itzhak, R. *et al.* Exciton Manipulation via Dielectric Environment Engineering in 2D Semiconductors. *ACS Appl. Opt. Mater.* **3**, 1330–1338 (2025).

53. Wangyang, P., Sun, H., Zhu, X., Yang, D. & Gao, X. Mechanical exfoliation and Raman spectra of ultrathin PbI₂ single crystal. *Mater. Lett.* **168**, 68–71 (2016).

54. Sinha, S. *et al.* Atomic structure and defect dynamics of monolayer lead iodide nanodisks with epitaxial alignment on graphene. *Nat. Commun.* **11**, 823 (2020).

55. Dugan, A. E. & Henisch, H. K. Fundamental optical absorption and photo-conduction in PbI₂ single crystals. *J. Phys. Chem. Solids* **28**, 1885–1890 (1967).

56. Bordas, J. & Davis, E. A. The excitons at the band edge of PbI₂. *Solid State Commun.* **12**, 717–720 (1973).

57. Ambardar, S., Yang, X. & Gao, J. Uncovering upconversion photoluminescence in layered PbI₂ above room temperature. *Sci. Rep.* **14**, 26900 (2024).

58. Fan, Q. *et al.* Liquid Exfoliation of Two-Dimensional PbI₂ Nanosheets for Ultrafast Photonics. *ACS Photonics* **6**, 1051–1057 (2019).

59. Wickramaratne, D., Weston, L. & Van de Walle, C. G. Monolayer to Bulk Properties of Hexagonal Boron Nitride. *J. Phys. Chem. C* **122**, 25524–25529 (2018).

60. Abdi, M., Chou, J.-P., Gali, A. & Plenio, M. B. Color Centers in Hexagonal Boron Nitride Monolayers: A Group Theory and Ab Initio Analysis. *ACS Photonics* **5**, 1967–1976 (2018).

61. Kahn, A. Fermi level, work function and vacuum level. *Mater. Horiz.* **3**, 7–10 (2016).

62. Li, D. *et al.* Manipulating the Self-Trapped Excitons in the Lead Iodide/Hexagonal Boron Nitride van der Waals Heterostructures. *Laser Photonics Rev.* **17**, 2300309 (2023).

63. Lifshitz, E., Bykov, L. & Yassen, M. An Optically Detected Magnetic Resonance Study of Laser Ablation Grown PbI₂ Epitaxial Films. *J. Phys. Chem.* **99**, 15262–15268 (1995).

64. Gottscholl, A. *et al.* Initialization and read-out of intrinsic spin defects in a van der Waals crystal at room temperature. *Nat. Mater.* **19**, 540–545 (2020).

65. Whitefield, B., Toth, M., Aharonovich, I., Tetienne, J.-P. & Kianinia, M. Magnetic Field Sensitivity Optimization of Negatively Charged Boron Vacancy Defects in hBN.
<https://doi.org/10.1002/qute.202300118> doi:10.1002/qute.202300118.

66. Novoselov, K. S. *et al.* Electric Field Effect in Atomically Thin Carbon Films. *Science* **306**, 666–669 (2004).
67. Purdie, D. G. *et al.* Cleaning interfaces in layered materials heterostructures. *Nat. Commun.* **9**, 5387 (2018).
68. Nonnenmacher, M., O’Boyle, M. P. & Wickramasinghe, H. K. Kelvin probe force microscopy. *Appl. Phys. Lett.* **58**, 2921–2923 (1991).
69. Andany, S. H. *et al.* An atomic force microscope integrated with a helium ion microscope for correlative nanoscale characterization. *Beilstein J. Nanotechnol.* **11**, 1272–1279 (2020).
70. Hosseini, N. *et al.* A polymer–semiconductor–ceramic cantilever for high-sensitivity fluid-compatible microelectromechanical systems. *Nat. Electron.* **7**, 567–575 (2024).
71. Sugawara, Y. *et al.* High potential sensitivity in heterodyne amplitude-modulation Kelvin probe force microscopy. *Appl. Phys. Lett.* **100**, 223104 (2012).